Applying Nyquist's Method for Stability Determination to Solar Wind Observations

Kristopher G. Klein[1,2] Justin C. Kasper[1] K.E. Korreck[3] Michael L.Stevens[3]

[1]Climate & Space Sciences & Engineering,University of Michigan, Ann Arbor MI, 48109 USA
[2]Lunar & Planetary Laboratory, University of Arizona, Tucson, AZ 85721 USA
[3]Smithsonian Astrophysical Observatory, 60 Garden Street, Cambridge, MA, 02138 USA

Key Points:

- An efficient and automated algorithm for the general determination of solar wind stability is presented
- This method agrees with traditional stability calculations, including for systems with multiple sources of free energy
- This method will be applied to future observations as a method for rapid determination of solar wind stability

Corresponding author: Kristopher G. Klein, `kriskl@umich.edu`

Abstract

The role instabilities play in governing the evolution of solar and astrophysical plasmas is a matter of considerable scientific interest. The large number of sources of free energy accessible to such nearly-collisionless plasmas makes general modeling of unstable behavior, accounting for the temperatures, densities, anisotropies, and relative drifts of a large number of populations, analytically difficult. We therefore seek a general method of stability determination that may be automated for future analysis of solar wind observations. This work describes an efficient application of the Nyquist instability method to the Vlasov dispersion relation appropriate for hot, collisionless, magnetized plasmas, including the solar wind. The algorithm recovers the familiar proton temperature anisotropy instabilities, as well as instabilities that had been previously identified using fits extracted from in situ observations in *Gary et al.* [2016]. Future proposed applications of this method are discussed.

1 Introduction

The solar wind, a hot, diffuse, and magnetized plasma, fills the heliosphere. Its low density and high temperature ensure that the charged particles which constitute the plasma experience few collisions from the time they are accelerated from the Sun's surface to the time they flow past the Earth; this weak collisionality allows the system to persist in a state far from local thermodynamic equilibrium. The deviations from LTE, which take the form of anisotropies between temperatures parallel and perpendicular to the mean magnetic field, relative drifts between the protons, electrons, and minor ions, ring distributions, and more general agyrotropic particle distributions, can serve as sources of free energy that may drive unstable behavior. The study of this menagerie of instabilities has a long and rich history in plasma and space physics, which we do not review here. *Gary* [1993] is a classic reference describing instabilities relevant to the solar wind, which can be supplemented with a modern review presented in *Yoon* [2017].

Work over the last decade using statistical sets of in situ solar wind observations indicate that instabilities act to govern the evolution of the solar wind. [*Kasper et al.*, 2002; *Hellinger et al.*, 2006; *Matteini et al.*, 2007; *Bale et al.*, 2009; *Maruca et al.*, 2011; *Chen et al.*, 2016] The prototypical example of these studies focuses on histograming observations onto a reduced parameter space, e.g. the proton parallel plasma $\beta_{||p} = 8\pi n_p T_{||p}/B^2$ versus proton temperature anisotropy $T_{\perp p}/T_{\parallel p}$ plane. By counting the number of observations, or the average value of a third quantity, in different regions of this parameter space, and comparing to modeled marginal instability thresholds, inferences can be made as to the action of instabilities in governing the solar wind's evolution. In the $(\beta_{||p}, T_{\perp p}/T_{\parallel p})$ case, stability thresholds derived for the mirror instability and the Alfvén (or oblique) firehose instability limit the observed distribution of plasma with $T_{\perp p} > T_{\parallel p}$ and $T_{\perp p} < T_{\parallel p}$ respectively. However, as discussed in *Hellinger and Trávníček* [2014], such conclusions may be complicated by the nature of such projections, which reduce a high-dimensional system to a two-dimensional space, obfuscating the effects of other plasma or solar wind parameters. Importantly, the stability thresholds used in these studies typically consider only a single source of free energy, neglecting the effects of additional sources, e.g. electron or minor ion drifts or anisotropies, which may act to stabilize or destabilize the system. Recent work by *Chen et al.* [2016] does account for the total contribution to the parallel and perpendicular pressure from each plasma component, but is limited to large-wavelength instabilities.

Rather than modeling the stability of a hot and magnetized plasma equilibrium for distinct sources of free energy, we develop in this work a more general method for stability determination, first described by *Nyquist* [1932]. Nyquist's method determines for a given dispersion relation and equilibrium parameters the number of normal mode solutions that have a positive growth rate. The method is employed in engineering contexts

[*Phillips et al.*, 1947], and has been applied to specific plasma physics cases as far back as the 1950's [*Jackson*, 1958; *Buneman*, 1959; *Penrose*, 1960; *Gardner*, 1963]. In this work, we demonstrate that Nyquist's method can be used to accurately and efficiently determine the stability of a plasma equilibrium with an arbitrary number of drifting ion and electron populations, each with a potentially unique bi-Maxwellian velocity distribution. The algorithm is described in Section 2, followed by a pedagogical application of the method to the well known proton-temperature anisotropy instabilities in Section 3. In Section 4, we apply the method to six intervals measured by the Wind spacecraft, first considered by *Gary et al.* [2016], as a test of the application of this method to actual solar wind observations. Proposed future uses of this method, including assisting event selection for data downloaded from *Parker Solar Probe* and extensions beyond the bi-Maxwellian framework, are described in Section 5.

2 Methodology

Nyquist's method was initially developed to study instabilities due to feedback in electronic circuits [*Nyquist*, 1932]. This method, as well as a simplification of the method made by *Penrose* [1960], are frequently described in plasma textbooks for the cases of simple electrostatic and electromagnetic equilibrium [*Krall and Trivelpiece*, 1973; *Stix*, 1992]. We therefore provide a brief review of the method, leaving aside proofs of the underlying complex analysis to other references (see §9.6 of *Krall and Trivelpiece* [1973] for further details).

For a general linearized system, frequency and wavevectors that satisfy the dispersion relation $|D(\omega, \gamma; \mathbf{k})| = 0$ describe the system's normal mode response to an initial perturbation; ω and γ are the real and imaginary components of the frequency and $\mathbf{k}$ is the wavevector. Normal modes with $\gamma < 0$ damp with increasing time, while those with $\gamma > 0$ are unstable and grow with time. Nyquist's key insight into studying these systems was that a contour integral of $|D|^{-1}$ over the upper-half complex-frequency plane will encircle all modes with $\gamma > 0$, allowing a straight-forward application of the residue theorem to count the number of singularities, and therefore the number of unstable modes. It can be shown that an equivalent method of evaluating this contour integral is to map the value of $|D|^{-1}$ along the line from $(\omega \to -\infty, \gamma = 0)$ to $(\omega \to +\infty, \gamma = 0)$ to a parametric curve in $(|D|_R^{-1}, |D|_I^{-1})$ space where R and I identify the real and imaginary components of the complex valued $|D|^{-1}$. Plots of this parametric curve are known as a "Nyquist diagram". The number of times this curve encircles the origin $(|D|_R^{-1}, |D|_I^{-1}) = (0, 0)$, an integer defined as the winding number W_n, equals the number of unstable normal modes the system supports.

To automate the counting of the winding number for an arbitrary parametric curve, we employ well-established algorithms from applied mathematics [*Shimrat*, 1962; *Hormann and Agathos*, 2001]. For a given curve, we identify all of the zeros where the curve crosses $|D|_I^{-1} = 0$, determine the handedness of the curve at each crossing, and add to or subtract from the value of W_n. For each left-handed crossing, $|D|_R^{-1} < 0$ and $|D|_I^{-1}$ changes from negative to positive or $|D|_R^{-1} > 0$ and $|D|_I^{-1}$ changes from positive to negative, we add 0.5 to W_n; For every right-handed crossing, $|D|_R^{-1} > 0$ and $|D|_I^{-1}$ changes from negative to positive or $|D|_R^{-1} < 0$ and $|D|_I^{-1}$ changes from positive to negative, we subtract 0.5 from W_n. To account for the behavior at large frequencies, we add 0.5 (-0.5) to W_n if $|D|_I^{-1}(\omega \to -\infty)$ is negative (positive). We note that W_n must be an integer; non-integer results signify an algorithmic error. The final value of W_n including all contributions from the $|D_I|^{-1} = 0$ crossings represents the number of unstable normal modes supported by the dispersion relation and equilibrium parameters under consideration.

For this work, we model the solar wind as a collection of an arbitrary number of drifting ion and electron populations, each with potentially unique bi-Maxwellians velocity distributions. We use the Plasma in a Linear Uniform Magnetized Environment (PLUME)

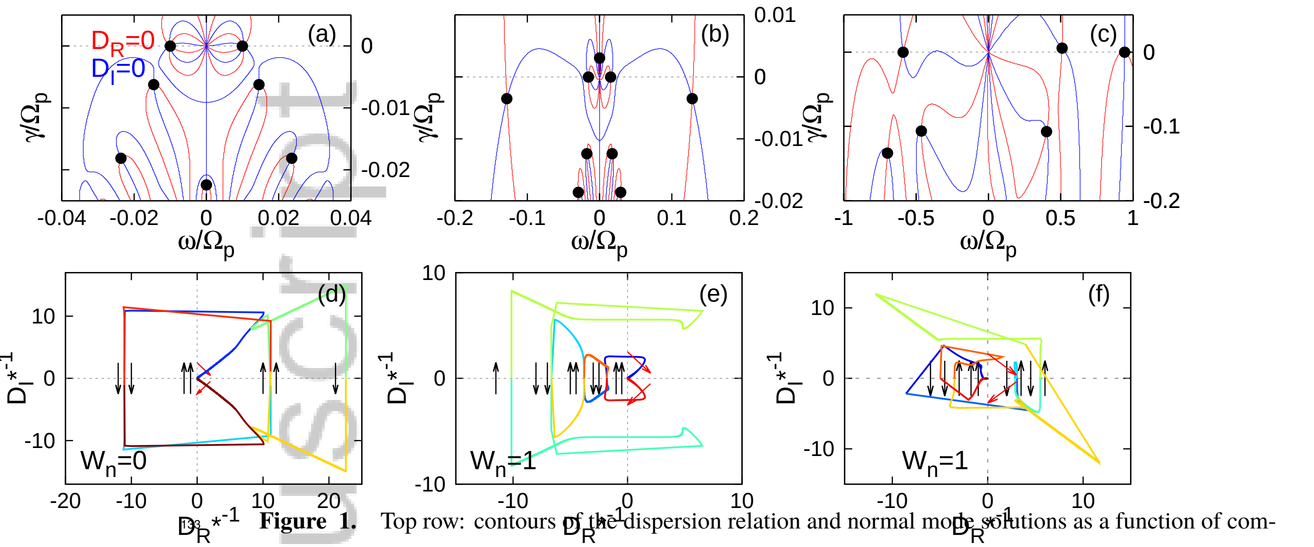

Figure 1. Top row: contours of the dispersion relation and normal mode solutions as a function of complex frequency (ω, γ) for a stable case, panel a, and two unstable cases, panels b and c. Bottom row: Nyquist diagrams, parametric curves of $D^{*-1}_{R,I} = \mathrm{sign}(|D|^{-1}_{R,I}) \log_{10}(1 + \mathrm{abs}|D|^{-1}_{R,I})$ evaluated along the $\gamma = 0$ line in complex frequency space, for the same three cases, with arrows indicating the handedness of the curve as it crosses $|D|^{-1}_{I} = 0$ and the associated W_n. Plasma parameters for the three cases are given in the text.

dispersion relation to supply values for $|D|$ [*Klein and Howes*, 2015]. PLUME numerically evaluates the plasma dispersion relation as derived in Chapter 10 of *Stix* [1992]. The dispersion relation depends on four global dimensionless parameters; the wavevectors parallel and perpendicular to the mean magnetic field $k_\perp \rho_R$ and $k_\parallel \rho_R$, the reference plasma $\beta_{\parallel R}$, and the relativistic factor $w_{||R}/c$, as well as six dimensionless parameters for each species; the density ratio n_s/n_R, the temperature ratio $T_{\parallel s}/T_{\parallel R}$, the temperature anisotropy $T_{\perp s}/T_{\parallel s}$, the mass ratio m_s/m_R, the charge ratio q_s/q_R, and the drift velocity in the reference species center of mass frame V_s/v_{AR}. The thermal gyroradius of species s, $\rho_s = w_{\perp s}/\Omega_s$, is defined as the ratio of the perpendicular thermal speed $w_{\perp s} = \sqrt{2k_B T_{\perp s}/m_s}$ over the species gyrofrequency $\Omega_s = q_s B/m_s c$ and the Alfvén velocity of species s is defined as $v_{As} = B/\sqrt{4\pi n_s m_s}$. Terms with the subscript R identify quantities calculated using the reference species, which is user-defined but typically selected to be the most abundant ion species in a system. For a plasma modeled with N components, the dispersion relation depends on $4 + 6 \times N - 5$ parameters. For all systems but the simplest isotropic proton-electron plasma, stability depends on complicated interactions between a large number of energy sources and sinks, motivating our automated treatment of stability analysis.

We illustrate in Fig. 1 three examples of the typical normal mode identification process as well as our Nyquist method algorithm. For the first example, we consider an isotropic proton-electron plasma with $\beta_p = 1.0$, $T_p = T_e$ and $(k_\perp, k_\parallel)\rho_p = (10^{-3}, 10^{-2})$. For the second example, we consider a proton-electron plasma with $\beta_{\parallel p} = 1.5$, $T_{\parallel p} = T_{\parallel e}$, $T_{\perp p}/T_{\parallel p} = 2.0$, $T_{\perp e}/T_{\parallel e} = 1.0$ and $(k_\perp, k_\parallel)\rho_p = (10^{-1}, 2 \times 10^{-2})$, the parameters for case c in Section 3. For the final example, we consider the four component plasma, comprised of proton core, proton beam, He^{2+} (α), and electron populations, with plasma parameters taken from Event 1 in *Gary et al.* [2016], described further in Section 4, and $(k_\perp, k_\parallel)\rho_p = (10^{-3}, 4 \times 10^{-1})$.

In the top row of Fig. 1, we present the contours $|D|_R = 0$ and $|D|_I = 0$ as a function of complex frequency. Intersections of these contours, where $|D| = 0$, locate normal mode solutions, which are indicated by black dots. By inspection, we see that panel a only has solutions with $\gamma < 0$, while panels b and c each have one solution with $\gamma > 0$, for the range of complex frequencies illustrated. Typical instability analysis using dispersion relations will identify an unstable mode in the (ω, γ) plane, and use that frequency as an initial guess as system parameters, such as $\mathbf{k}$ or $T_{\perp p}/T_{\parallel p}$, are varied in a nearly continuous fashion. This type of analysis can be very insightful, but it relies on either a good initial guess for the normal mode frequency, or the application of a root-finding routine over some range of user-defined frequencies, and can be susceptible to misidentification of roots or to root-jumping if the variation of system parameters for a scan is too large.

In the bottom row of Fig. 1, we present Nyquist diagrams for same three examples as an illustration of our instability identification method. For each case, we calculate the parametric curve $[|D|_R^{-1}, |D|_I^{-1}](\omega, \gamma_0 = 0)$. The large frequency limit of $|\omega| = \omega_{\max}$ is selected so that $\xi_s = (\omega - V_s)/k_\parallel w_{\parallel s}$ is larger than 10 for all plasma components. [1] Values for the parametric curve are calculated for log-spaced frequencies between $-\omega_{\max}$ and $-|\omega_{\min}| = -10^{-6}\Omega_p$ and between $\omega_{\min}$ and $\omega_{\max}$ at a total of 4000 points. A bisection algorithm is employed to identify all $|D|_I^{-1} = 0$ crossings, which may fall between the initially-selected frequency points. The handedness of the curve, as described earlier in this section, is also calculated at each crossing and used in calculating W_n. In panels d-f, we plot the contours of $D_j^{*-1} = \mathrm{sign}(|D|_j^{-1}) \log_{10}(1 + \mathrm{abs}|D|_j^{-1})$. The color of the contour changes for each crossing of $|D|_I^{-1} = 0$. To help elucidate these examples, a black arrow is drawn near each crossing with the same sign of $|D|_R^{-1}$ and same handedness as the parametric curve. Each black arrow with $|D|_R^{-1} < 0$ pointed upward or $|D|_R^{-1} > 0$ pointed downward adds 0.5 to W_n, while each black arrow with $|D|_R^{-1} < 0$ pointed downward or $|D|_R^{-1} > 0$ pointed upward subtracts 0.5 from W_n. [2] As the parametric curve does not cross zero for $\omega \to \pm\infty$, we illustrate with red arrows the behavior of the curve for the two large frequency limits. For all three cases shown, $|D|_I^{-1}(\omega \to -\infty) < 0$ and $|D|_I^{-1}(\omega \to \infty) > 0$, resulting in a left-handed encirclement, adding 0.5 to W_n. Accounting for the handedness of zero-crossings and large ω limits produces a winding number of 0, 1, and 1 respectively for the three examples, which is identical to the number of unstable modes supported by each equilibrium.

Unlike typical dispersion relation analysis, the winding number calculation does not provide any information about the normal modes, such as their frequency, growth rate, or eigenfunction polarizations. It simply identifies the number of unstable modes supported by a particular system. However, the winding number calculation can be applied generally and automatically, without any intelligent selection of modes that are or will become unstable due to parameter variation, and without the concern of mode misidentification or the solution jumping to a different normal mode. Additionally, the Nyquist curve can be calculated using any constant value of γ; that is, instead of calculating the winding number from the $[|D|_R^{-1}, |D|_I^{-1}](\omega, \gamma_0 = 0)$ curve, and thus how many normal modes have a growth rate greater than $\gamma = 0$, we can calculate the winding number from the $[|D|_R^{-1}, |D|_I^{-1}](\omega, \gamma_0 \neq 0)$ curve, yielding the number of normal modes that have a growth rater greater than $\gamma = \gamma_0$. As we will see in the following section, this allows us to high-

[1] The term ξ_s is the argument of the plasma dispersion function Z used to evaluate the Landau integrals in the dispersion relation [*Fried and Conte*, 1961]. The large values of ion to electron mass ratios ensure that for $\xi_e = 10$, we will resolve ion-cyclotron resonant behavior. For future studies of instabilities involving electron-cyclotron behavior, larger values of ξ_e must be considered.

[2] The complementary function D_j^{*-1} is necessary to illustrate these curves due to the large range of values for $|D|^{-1}$ natural to our systems; the structure of D_j^{*-1} preserves the zero crossings and signs of both components of $|D|$, making it ideal for visualizing the Nyquist diagram.

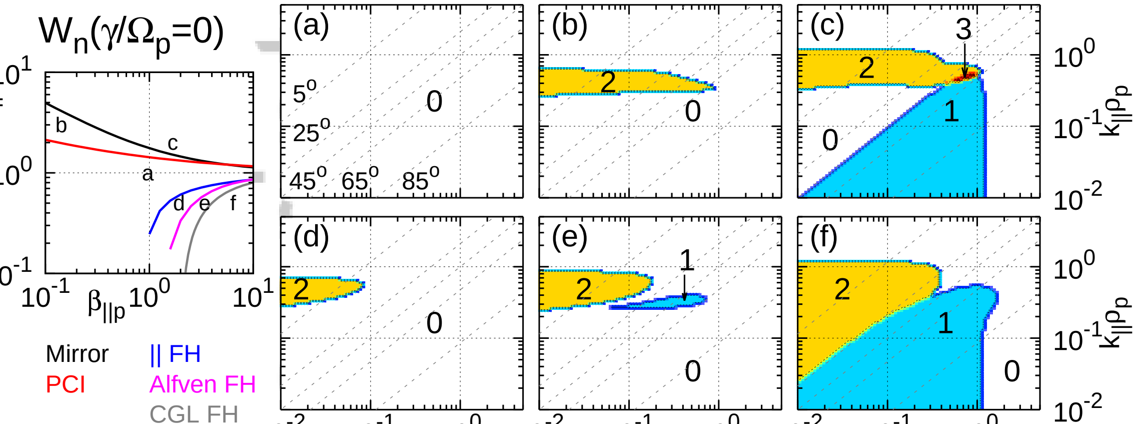

Figure 2. The winding number as a function of $(k_\perp\rho_p, k_\|\rho_p)$ calculated at six points in the $(\beta_{\|p}, T_{\perp p}/T_{\|p})$ plane, indicated in relation to marginal stability thresholds in the left panel. A stable wavenumber is indicated in white, a wavenumber with one unstable mode in blue, two in yellow, and three in red.

light unstable modes which will grow fast enough to affect the dynamics of our systems of interest.

3 A Pedagogical Example

As a first test of our algorithm, we consider the well-known proton-temperature anisotropy driven instabilities. We calculate W_n at six points in $(\beta_{\|p}, T_{\perp p}/T_{\|p})$ space for a proton-electron plasma, with $T_{\|p} = T_{\|e}$ and $T_{\perp e} = T_{\|e}$. The six points, illustrated in the left panel of Fig. 2, are selected so that we consider a stable case, and a case beyond each of the five marginal stability thresholds. We use values from Table 1 in *Verscharen et al.* [2016] with a threshold value of $\gamma_{\rm th} = 10^{-3}\Omega_p$ for the mirror, ion cyclotron, parallel firehose, and Alfvén firehose instabilities; the CGL (or fluid) firehose threshold is simply $T_{\perp p}/T_{\|p} = 1 - 2\beta_{\|p}^{-1}$. For each value of $(\beta_{\|p}, T_{\perp p}/T_{\|p})$, we calculate W_n over a 128^2 point wavevector grid with $k_\perp\rho_p$ and $k_\|\rho_p$ ranging from 10^{-2} to 10^1. For comparison, we draw the reader's attention to Fig. 2 in *Klein and Howes* [2015], which plots the growth rate of unstable modes as a function of $\mathbf{k}$ in a similar fashion to Fig. 2.

For the stable equilibrium, case a, W_n is zero over the entire wavevector plane, as expected for a system with no unstable modes. For case b, with $(\beta_{\|p}, T_{\perp p}/T_{\|p}) = (0.15, 3.0)$, W_n is zero for most $\mathbf{k}\rho_p$, but is equal to 2 over a narrow band of parallel wavevectors. This is the wavevector region where the proton-cyclotron instability arises. An increase in $\beta_{\|p}$ for case c, to $(\beta_{\|p}, T_{\perp p}/T_{\|p}) = (1.5, 2.0)$, both expands the proton-cyclotron unstable wavevector region and drives the mirror instability for more oblique wavevectors. We can distinguish between the two types of instabilities based upon the number of modes driven unstable; the proton-cyclotron instability drives both a forward and backward propagating Alfvén wave, resulting in $W_n = 2$, while only one non-propagating mode is driven by the mirror instability, resulting in $W_n = 1$ for modes with $k_\perp > k_\|$. The small region with $W_n = 3$ indicates wavevectors unstable to both the mirror and proton-cyclotron instabilities.

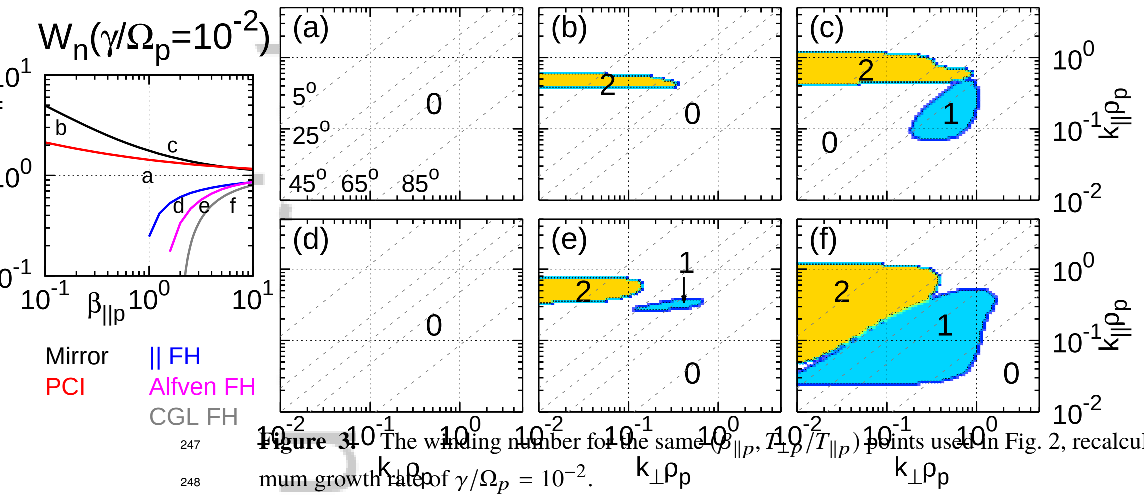

Figure 3. The winding number for the same $(\beta_{\parallel p}, T_{\perp p}/T_{\parallel p})$ points used in Fig. 2, recalculated for a minimum growth rate of $\gamma/\Omega_p = 10^{-2}$.

For the three $T_{\perp p} < T_{\parallel p}$ cases, cases d-f, we keep $T_{\perp p}/T_{\parallel p} = 0.5$ constant and vary $\beta_{\parallel p}$ from 2.0 to 3.0 to 6.0. For case d, we find $W_n = 2$ over the wavevector region where the parallel firehose instability is known to drive unstable forward and backward propagating magnetosonic waves. For case e, the $W_n = 2$ parallel firehose region is expanded, and we also recover the Alfvén firehose instability, which drives a single non-propagating Alfvén mode at oblique wavevectors. For the highest $\beta_{\parallel p}$ case, case f, both the parallel and Alfvén firehose unstable regions have expanded to include nearly all wavevectors with $|k|\rho_p < 1$. This $(\beta_{\parallel p}, T_{\perp p}/T_{\parallel p})$ point satisfies the CGL instability criteria, and thus in the large wavevector limit, the Vlasov solution agrees with instability predictions from MHD. For all six cases, our algorithm is able to correctly calculate both where in wavevector space unstable modes are driven and the number of unstable modes.

As previously noted, the Nyquist method does not produce any characteristics of the unstable modes; values of W_n as a function of wavevector do not distinguish between slowly and quickly growing instabilities. However, we are able to calculate $W_n(k_\perp\rho_p, k_\parallel\rho_p)$ using a contour integral with any arbitrary value of $\gamma = \gamma_0$, with the resulting integer reporting the number of modes with $\gamma > \gamma_0$. In Fig. 3, we repeat the winding number calculations at the same six points in $(\beta_{\parallel p}, T_{\perp p}/T_{\parallel p})$ space used for Fig. 2, replacing $\gamma_0 = 0$ with $\gamma_0 = 10^{-2}\Omega_p$. The stable case, case a, has $W_n = 0$ for all wavevectors. Cases b and c have significant reductions in the wavevector regions which have non-zero W_n. By comparing the $\gamma_0 = 0$ and $\gamma_0 = 10^{-2}\Omega_p$ cases, we see that a significant fraction of the wavevectors unstable to the mirror mode, especially with large wavevectors, have weak growth rates. This is not a novel finding, but a novel means of identifying regions of unstable modes with sufficiently large growth rates.

We see similar reductions for the $T_{\perp p} < T_{\parallel p}$ cases. The parallel firehose instability is relatively weak for case d, with no wavevectors having growth rates larger than $10^{-2}\Omega_p$. For cases e and f, there are some reductions in the extent of the unstable wavevector regions, especially for case f in the small $k_\parallel$, or large wavevector, limit.

As this method is intended for eventual application to analysis of a large number of observations, we would like to calculate W_n at fewer than $128^2 = 16384$ wavevectors

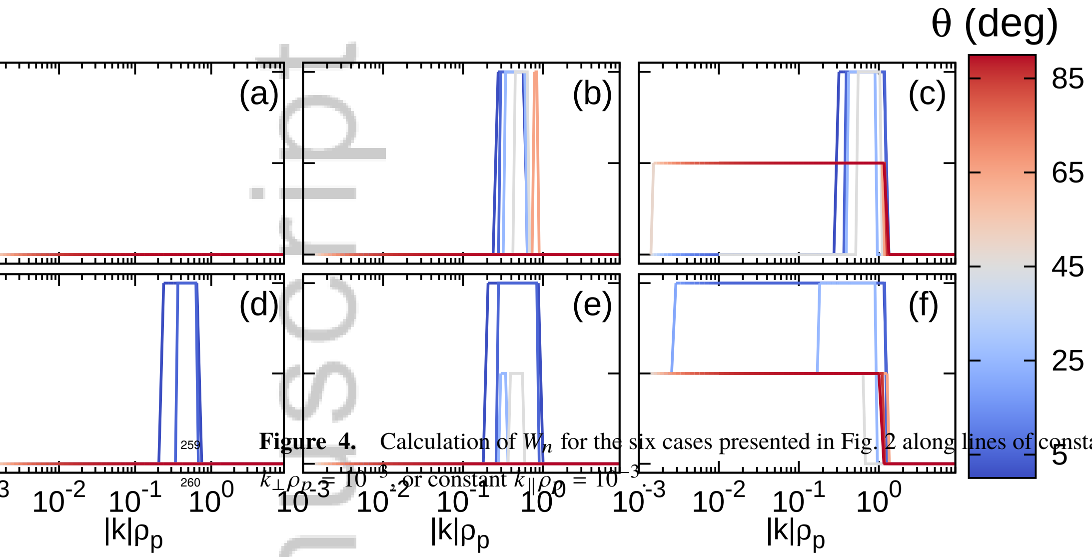

Figure 4. Calculation of W_n for the six cases presented in Fig. 2 along lines of constant angle, constant $k_\perp \rho_p = 10^{-3}$, or constant $k_\parallel \rho_p = 10^{-3}$.

and still determine if the system supports any unstable modes. We take advantage of the preference for unstable modes to occur for wavevectors satisfying $k_\perp \ll k_\parallel$, $k_\perp \approx k_\parallel$, and $k_\perp \gg k_\parallel$ and calculate W_n along seven paths; constant $k_\perp \rho_p = 10^{-3}$, constant $k_\parallel \rho_p = 10^{-3}$, and $\theta = \mathrm{atan}\left(k_\perp / k_\parallel\right) \in [5, 25, 45, 65, 85]^\circ$. The paths of constant θ are illustrated in Figs. 2 and 3 as grey dashed lines. In Fig. 4, we plot W_n calculated for 128 points in $|k|\rho_p$ along the seven paths for the six $(\beta_{\parallel p}, T_{\perp p}/T_{\parallel p})$ cases. The results are consistent with the full wavevector scans, and illustrate that we are able to capture the presence and structure of these temperature anisotropy instabilities with significantly fewer calculations.

4 Application to WIND Observations

We next turn to an application of the Nyquist method to in situ solar wind observations. *Gary et al.* [2016] selected six intervals from the Wind measurements from March 19, 2005 which were associated which enhanced magnetic fluctuations. Using data from the magnetometer [*Lepping et al.*, 1995], the SWE Faraday cup [*Ogilvie et al.*, 1995] and electrostatic analyzer [*Lin et al.*, 1995], bi-Maxwellian fits of a proton core and beam, alpha particles, and electrons were constructed, with parameters given in their Table 1. Using the fit parameters of the four plasma populations, they performed a normal mode analysis of the six intervals, and found parallel propagating instabilities associated with five of the intervals. In this section, we repeat their normal mode analysis, as well as calculate the winding number associated with the observed equilibrium.

In the top row of Fig. 5, we plot the imaginary component of the normal mode frequency of the fast/magnetosonic and Alfvén waves associated with the six selected events as a function of $k_\parallel \rho_p$ for constant $k_\perp \rho_p = 10^{-3}$. The drifting proton beam and α particles break the $\omega = -\omega$ symmetry found in systems with no drifts, leading to different dispersion relations for Sunward and anti-Sunward propagating waves. Stable damping rates are plotted as dashed lines, while unstable growth rates are plotted with solid lines. As was reported in *Gary et al.* [2016], no unstable mode was identified for Event # 3, and the instabilities we find for Events # 1, 2, 6, and 7 are the same as described in the previous work. For Event # 4, we located one of the two instabilities reported in *Gary et al.* [2016].

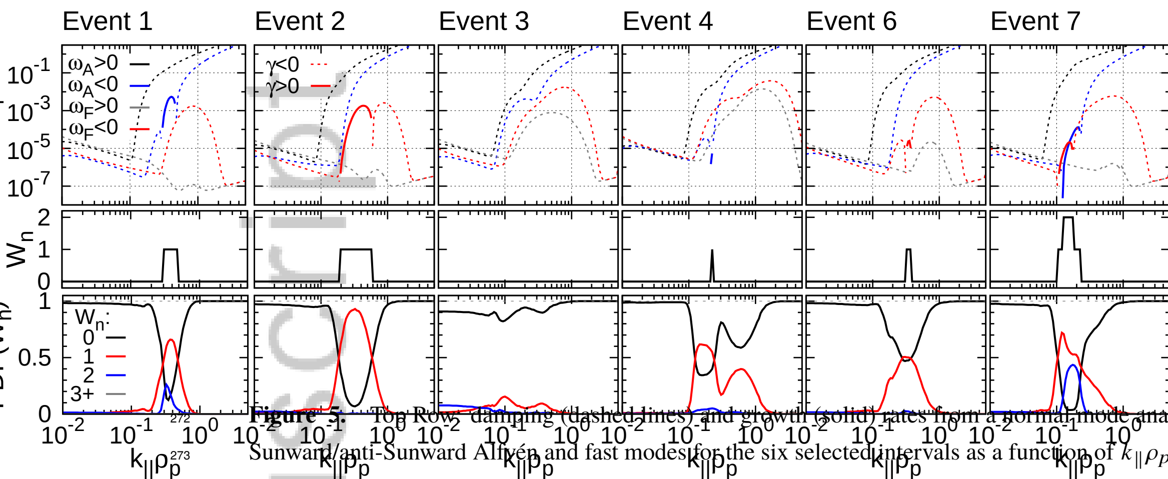

Figure 5. Top Row: damping (dashed lines) and growth (solid) rates from a normal mode analysis of the Sunward/anti-Sunward Alfvén and fast modes for the six selected intervals as a function of $k_\parallel \rho_p$. Center Row: The winding number for the same intervals, which is nonzero for the same wavevectors an unstable normal mode is identified. Bottom Row: Probability distribution functions of winding number extracted from a Monte Carlo randomization of the measured equilibrium plasma parameters.

The anti-sunward propagating magnetosonic mode is stable for the reported values in their Table 1; after correspondence with the authors, we believe an artificially large drift velocity for the α population was used in the calculation of their Fig. 7.

In the central row of Fig. 5, we plot $W_n(k_\parallel \rho_p)$, calculated using the same bi-Maxwellian fits for the four plasma populations used for the normal mode analysis. We see that $W_n = 0$ for all wavevectors with no unstable mode, and when one or more unstable mode is supported, the winding number matches the number of unstable modes; e.g. $W_n = 2$ for wavevectors for which both the anti-sunward propagating Alfvén and fast modes are unstable in Event # 7. This comparison demonstrates that calculation of W_n can determine if particular intervals of solar wind observations, and not just idealized systems with single sources of free energy, are linearly unstable.

As seen in Section 3, not all instabilities arise for wavevectors satisfying $k_\perp \ll k_\parallel$. In an attempt to determine if any of the observed events have instabilities with oblique wavevectors, we calculate W_n for the six events over a grid in $(k_\perp \rho_p, k_\parallel \rho_p)$, illustrated in Fig. 6. For the five unstable events, $W_n \neq 0$ only for the parallel wavevectors already identified in the scan of $k_\parallel$ presented in Fig. 5, and for Event # 3 no oblique instability is identified. Our algorithm for calculating W_n has allowed us to verify that only parallel instabilities are driven for the observed equilibrium.

We lastly consider how variations in the plasma equilibrium, introduced either through changes in the solar wind or errors in observation, may affect the stability of the system. For the six events, we perform a Monte Carlo variation of the observed dimensional quantities, namely population density, drift velocity, parallel and perpendicular temperature, as well as magnetic field amplitude. For each quantity F_0, we vary the quantity to a value randomly drawn from a Gaussian distribution centered at F_0 with standard deviation $0.1 \times F_0$. To ensure quasineutrality and zero-net current are maintained, the electron density and drift velocity are set using the values from the ion variation. For each instantiation of this procedure, $W_n(k_\parallel \rho_p)$ is recalculated. This procedure is repeated 1000 times

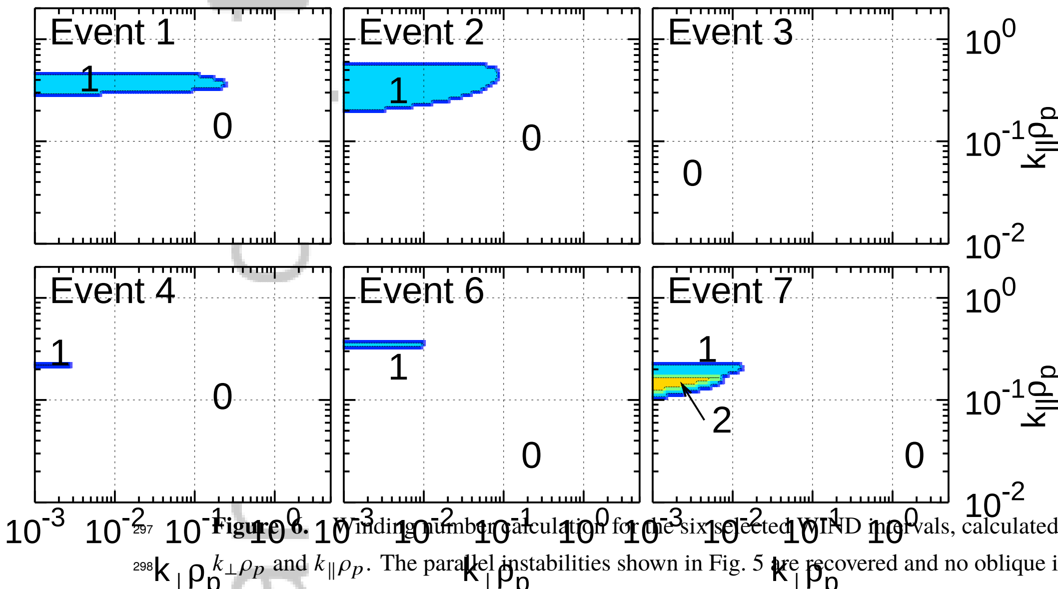

Figure 6. Winding number calculation for the six selected WIND intervals, calculated as a function of $k_{\perp}\rho_p$ and $k_{\parallel}\rho_p$. The parallel instabilities shown in Fig. 5 are recovered and no oblique instabilities are identified.

for each event, and the probability distribution function of W_n is displayed in the bottom row of Fig. 5.

We see that for Events # 1, 2 and 7, more than 90 % of the considered equilibrium are unstable, with the peak of the ensemble instability arising for the same wavevectors driven unstable for the observed equilibrium. The PDF of W_n for Event # 4 has a bi-modal distribution, with $\approx$ 60% of the ensemble unstable around $k_{\parallel}\rho_p = 0.1$ and $\approx$ 40% unstable around 0.4, a region of probable instability much wider than the relatively narrow observed region of instability. Further analysis calculating the energy transfer between the individual plasma components and the electromagnetic wave on selected unstable instances from the ensemble, not shown, finds that the two unstable regions are associated with resonant energy transfer from either the alpha or proton beam populations respectively. For Event # 3, only $\approx$ 20% of the ensemble is unstable, indicating that neither observational error in measuring the plasma nor small changes in the equilibrium are likely obscuring instabilities in the system. The efficient and automated nature of our Nyquist method algorithm allows for an assessment of the effects of measurement error on our ability to observe instabilities; for three of the events, the observed region of instability matches exactly with the probable region, for one event the same lack of instabilities is found, and for two events, a broader range of probable instabilities is identified.

5 Discussion and Conclusion

In this work, we provided a review of Nyquist's method for stability determination, with particular emphasis on its application to hot, diffuse, magnetized plasmas. Using the PLUME numerical dispersion relation solver, we implemented an efficient and automated algorithm for evaluating Nyquist's method, outputting an integer known as the winding number W_n which corresponds to the number of unstable modes supported by the system for an selected plasma equilibrium. This algorithm was tested against well known proton-temperature anisotropy instabilities as well as in situ observations of instabilities in the solar wind, and was found in agreement with the typical normal mode instability analysis.

One intended use for this algorithm is for NASA's *Parker Solar Probe* Mission (PSP), scheduled to launch in late 2018, that will make the first in situ measurements of solar wind plasma in the near-Sun environment [*Fox et al.*, 2015]. One of the key science questions for PSP is to "[d]etermine the structure and dynamics of the plasma and magnetic fields at the sources of the solar wind"; instabilities are likely to play a role in the dynamic phenomena of interest. The thermal plasma instruments on PSP which comprise the Solar Wind Electrons Alphas Protons (SWEAP) instrument suite consist of 4 sensors, a Faraday cup, two electron electrostatic analyzers and an ion electrostatic analyzer[*Kasper et al.*, 2015]. These instruments will measure the thermal plasma of the solar wind from 10 eV - 20 keV for protons and 5 eV - 30 keV for electrons. The data collected from this instrument suite will be down-linked in two parts. The first part will be a survey data that will sample the solar wind plasma at a 56 second cadence. These data will then be utilized to select full resolution data with a maximum cadence of 0.5 seconds to study the solar wind plasma in detail. To select an hours worth of data from over 10 days at closest approach to the Sun, the survey data will need to be examined to find the most scientifically relevant intervals. The method described in this paper will be utilized to help guide scientists in their identification of the data to select.

The survey data will be processed from raw form into a higher-level set that will include three species, protons, alphas, and electrons, and will provide the density, velocity and temperature for each. Using the SWEAP data combined with measurements of electric and magnetic fields from the Fields instrument suite [*Bale et al.*, 2016], other auxiliary data will be calculated including Alfvén speed, plasma β, and sound speed. The Nyquist method will then be run on the survey data, calculating the winding number using the 56 second survey data along the seven paths in wavevector space illustrated in Fig. 4. The winding number will be plotted with the observed plasma parameters and other derived quantities to allow scientists a way to identify the best high-cadence data to select for download.

Within this work, we have restricted ourselves to a bi-Maxwellian description of the plasma equilibrium. The Nyquist method does not generally have this restriction, and future studies will consider other dispersion relations with more accurate descriptions of the velocity distribution of the plasma. In particular, we intend to apply the Nyquist method to the numerical dispersion relation solver ALPS, the Arbitrary Linear Plasma Solver [*Verscharen et al.*, 2017], which produces a dispersion relation from direct numerical integration rather than the approximation of a particular analytic form of the velocity distribution. Differences between applications of the Nyquist method using PLUME and ALPS may help elucidate where departures from a Maxwellian description significantly affect the stability of a plasma.

The technique presented in this work will be useful for the study of the stability of a large number of plasma systems, in particular expanding our understanding of stability of plasmas within the canonical $(\beta_{\parallel p}, T_{\perp p}/T_{\parallel p})$ plane and exploring the impact of other sources of free energy and may be applied to measurements of the solar wind and planetary magnetospheres, as well as data sets derived from multi-fluid or kinetic numerical simulations. These applications will be considered in future work.

Acknowledgments

The authors would like to thank Peter Gary for insightful discussions concerning the *Wind* intervals selected for study in *Gary et al.* [2016]. The plasma parameters used for the W_n calculations in Section 4 can be found in Table 1 of *Gary et al.* [2016]. K.G. Klein was supported by NASA grant NNX16AG81G. J. C. Kasper, K. E. Korreck, M.L. Stevens acknowledge support from NASA under contract NNN06AA01C (Task NNN10AA08T) to the Smithsonian Astrophysical Observatory. M.L. Stevens was also supported by NASA grant NNX14AT26G.

References

Bale, S. D., J. C. Kasper, G. G. Howes, E. Quataert, C. Salem, and D. Sundkvist, Magnetic Fluctuation Power Near Proton Temperature Anisotropy Instability Thresholds in the Solar Wind, *Phys. Rev. Lett.*, *103*(21), 211101, 2009.

Bale, S. D., et al, The FIELDS Instrument Suite for Solar Probe Plus. Measuring the Coronal Plasma and Magnetic Field, Plasma Waves and Turbulence, and Radio Signatures of Solar Transients, *Space Sci. Rev.*, *204*, 49–82, 2016.

Buneman, O., Dissipation of currents in ionized media, *Phys. Rev.*, *115*, 503–517, 1959.

Chen, C. H. K., L. Matteini, A. A. Schekochihin, M. L. Stevens, C. S. Salem, B. A. Maruca, M. W. Kunz, and S. D. Bale, Multi-species Measurements of the Firehose and Mirror Instability Thresholds in the Solar Wind, *Astrophys. J. Lett.*, *825*, L26, 2016.

Fox, N. J., et al., The Solar Probe Plus Mission: Humanity's First Visit to Our Star, *Space Sci. Rev.*, 2015.

Fried, B. D., and S. D. Conte, *The Plasma Dispersion Function*, Academic Press, 1961.

Gardner, C. S., Bound on the Energy Available from a Plasma, *Physics of Fluids*, *6*, 839–840, 1963.

Gary, S. P., *Theory of Space Plasma Microinstabilities*, 1993.

Gary, S. P., L. K. Jian, T. W. Broiles, M. L. Stevens, J. J. Podesta, and J. C. Kasper, Ion-driven instabilities in the solar wind: Wind observations of 19 March 2005, *J. Geophys. Res.*, *121*, 30–41, 2016.

Hellinger, P., and P. M. Trávníček, Solar Wind Protons at 1 AU: Trends and Bounds, Constraints and Correlations, *Astrophys. J. Lett.*, *784*, L15, 2014.

Hellinger, P., P. Trávníček, J. C. Kasper, and A. J. Lazarus, Solar wind proton temperature anisotropy: Linear theory and WIND/SWE observations, *Geophys. Res. Lett.*, *33*, 9101, 2006.

Hormann, Kai, and Alexander Agathos, The point in polygon problem for arbitrary polygons, *Computational Geometry*, *20*(3), 131 – 144, 2001.

Jackson, J.D., *PLASMA OSCILLATIONS*, 1958.

Kasper, J. C., A. J. Lazarus, and S. P. Gary, Wind/SWE observations of firehose constraint on solar wind proton temperature anisotropy, *Geophys. Res. Lett.*, *29*(17), 1839, 2002.

Kasper, Justin C., et al., Solar wind electrons alphas and protons (sweap) investigation: Design of the solar wind and coronal plasma instrument suite for solar probe plus, *Space Sci. Rev.*, pp. 1–56, 2015.

Klein, K. G., and G. G. Howes, Predicted impacts of proton temperature anisotropy on solar wind turbulence, *Phys. Plasmas*, *22*(3), 032903, 2015.

Krall, N. A., and A. W. Trivelpiece, *Principles of plasma physics*, McGraw-Hill, 1973.

Lepping, R. P., M. H. AcÅĺna, L. F. Burlaga, W. M. Farrell, J. A. Slavin, K. H. Schatten, F. Mariani, N. F. Ness, F. M. Neubauer, Y. C. Whang, J. B. Byrnes, R. S. Kennon, P. V. Panetta, J. Scheifele, and E. M. Worley, The wind magnetic field investigation, *Space Sci. Rev.*, *71*, 207–229, 1995, 10.1007/BF00751330.

Lin, R. P.,et al., A Three-Dimensional Plasma and Energetic Particle Investigation for the Wind Spacecraft, *Space Sci. Rev.*, *71*, 125–153, 1995.

Maruca, B. A., J. C. Kasper, and S. D. Bale, What Are the Relative Roles of Heating and Cooling in Generating Solar Wind Temperature Anisotropies?, *Phys. Rev. Lett.*, *107*(20), 201101, 2011.

Matteini, L., S. Landi, P. Hellinger, F. Pantellini, M. Maksimovic, M. Velli, B. E. Goldstein, and E. Marsch, Evolution of the solar wind proton temperature anisotropy from 0.3 to 2.5 AU, *Geophys. Res. Lett.*, *34*, L20105, 2007.

Nyquist, Harry, Regeneration theory, *Bell system technical journal*, *11*(1), 126–147, 1932.

Ogilvie, K. W., D. J. Chornay, R. J. Fritzenreiter, F. Hunsaker, J. Keller, J. Lobell, G. Miller, J. D. Scudder, E. C. Sittler Jr., R. B. Torbert, D. Bodet, G. Needell, A. J. Lazarus, J. T. Steinberg, J. H. Tappan, A. Mavretic, and E. Gergin, SWE, A Comprehensive Plasma Instrument for the Wind Spacecraft, *Space Sci. Rev.*, *71*, 55–77, 1995.

Penrose, O., Electrostatic Instabilities of a Uniform Non-Maxwellian Plasma, *Physics of Fluids*, *3*, 258–265, 1960.

Phillips, Ralph S, Hubert M James, and Nathaniel B Nichols, *Theory of Servomechanisms*, Dover Publications, 1947.

Shimrat, M., Algorithm 112: Position of point relative to polygon, *Commun. ACM*, *5*(8), 434–, 1962.

Stix, T. H., *Waves in plasmas*, American Institute of Physics, 1992.

Verscharen, D., B. D. G. Chandran, K. G. Klein, and E. Quataert, Collisionless Isotropization of the Solar-wind Protons by Compressive Fluctuations and Plasma Instabilities, *Astrophys. J.*, *831*, 128, 2016.

Verscharen, D., K. G. Klein, B. D. G. Chandran, M. L. Stevens, C. S. Salem, and S. D. Bale, ALPS: The Arbitrary Linear Plasma Solver, *J. Plasma Phys.*, 2017.

Yoon, P.H., Kinetic instabilities in the solar wind driven by temperature anisotropies, *Rev. Mod. Phys.*, 2017.

Figure 1.

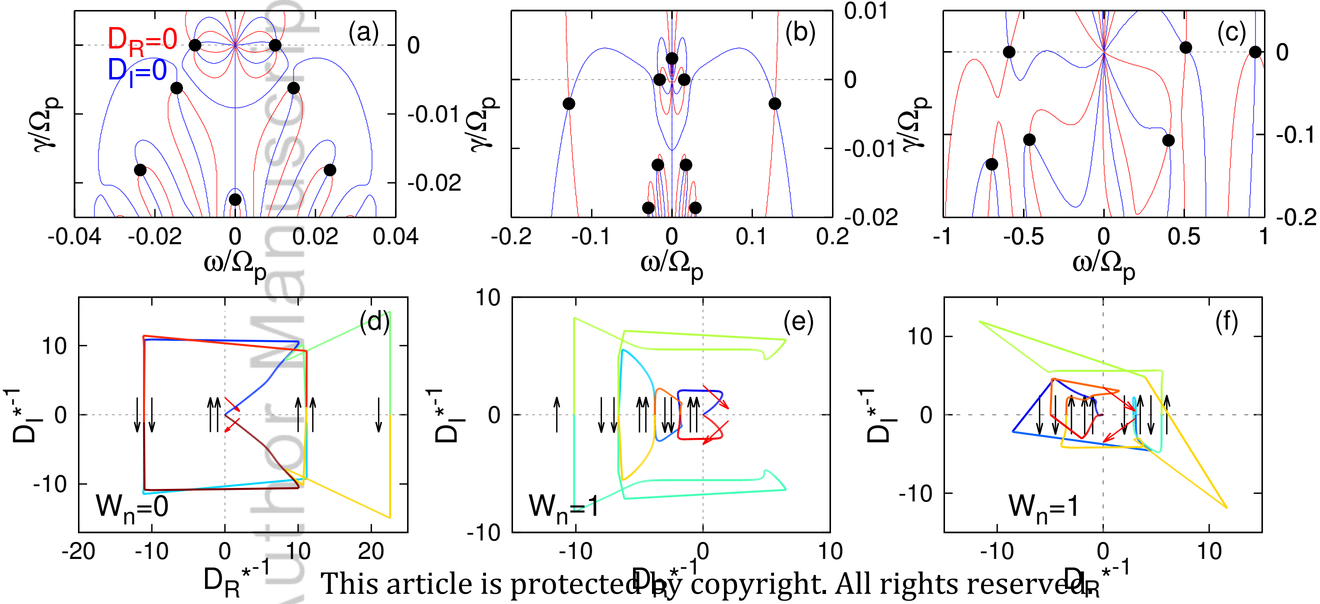

D_R=0
D_I=0
(a)
(b)
(c)
(d)
(e)
(f)
γ/Ω_p
ω/Ω_p
D_I^{*-1}
D_R^{*-1}
W_n=0
W_n=1
W_n=1

Figure 2.

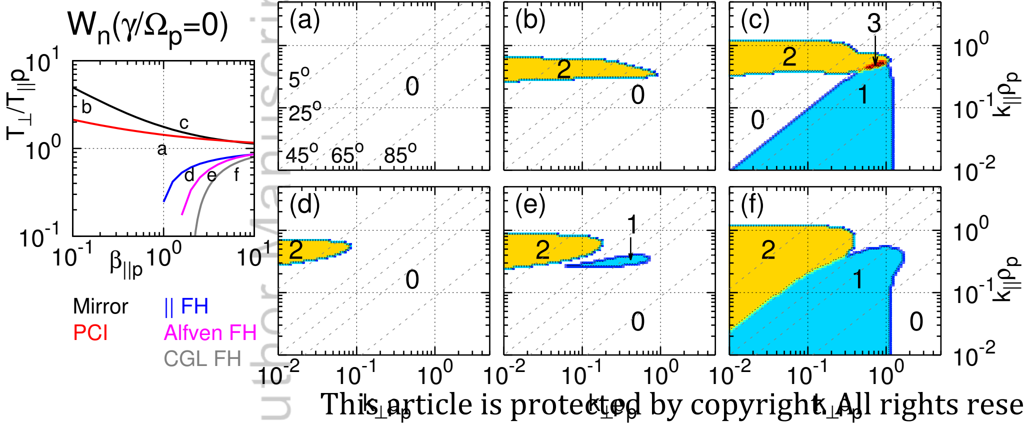

$W_n(\gamma/\Omega_p=0)$
$T_\perp/T_{||p}$
$\beta_{||p}$
a
b
c
d
e
f
Mirror
PCI
|| FH
Alfven FH
CGL FH
(a)
(b)
(c)
(d)
(e)
(f)
5°
25°
45°
65°
85°
0
1
2
3
$k_{||}\rho_p$
$k_\perp\rho_p$

Figure 3.

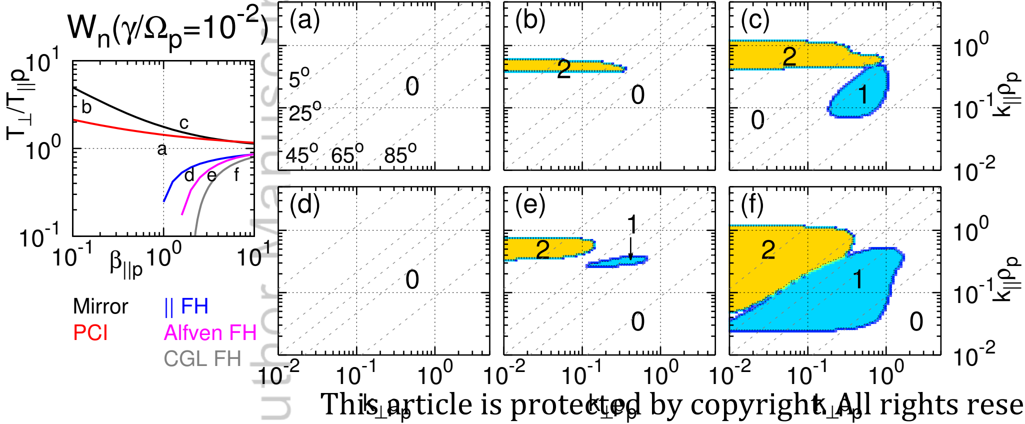

$W_n(\gamma/\Omega_p=10^{-2})$
$T_\perp/T_{\|p}$
$\beta_{\|p}$
Mirror
PCI
|| FH
Alfven FH
CGL FH
(a)
(b)
(c)
(d)
(e)
(f)
$k_\perp\rho_p$
$k_\|\rho_p$

Figure 4.

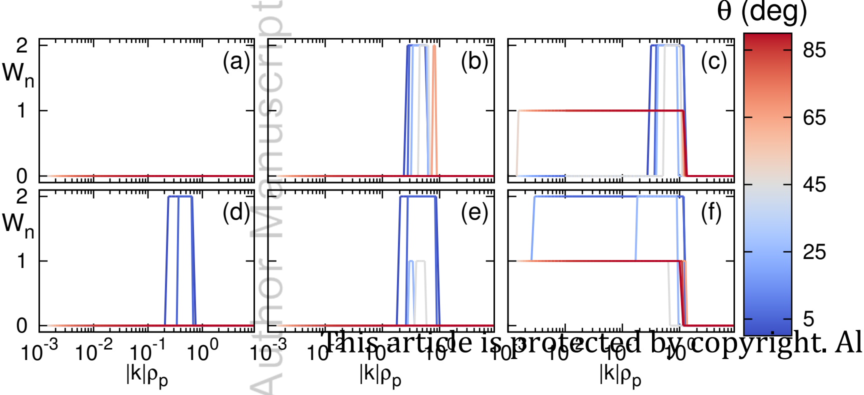
θ (deg)
85
65
45
25
5
2
1
0
W_n
(a)
(b)
(c)
(d)
(e)
(f)
10^-3
10^-2
10^-1
10^0
|k|ρ_p

Figure 5.

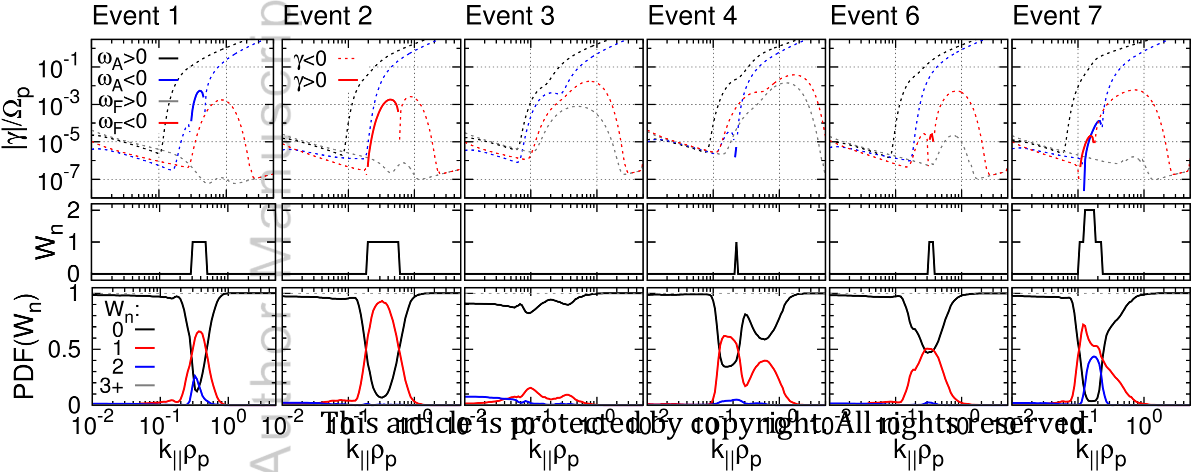

Event 1
Event 2
Event 3
Event 4
Event 6
Event 7
$|\gamma|/\Omega_p$
$\omega_A>0$
$\omega_A<0$
$\omega_F>0$
$\omega_F<0$
$\gamma<0$
$\gamma>0$
W_n
PDF(W_n)
W_n:
0
1
2
3+
$k_{||}\rho_p$

Figure 6.

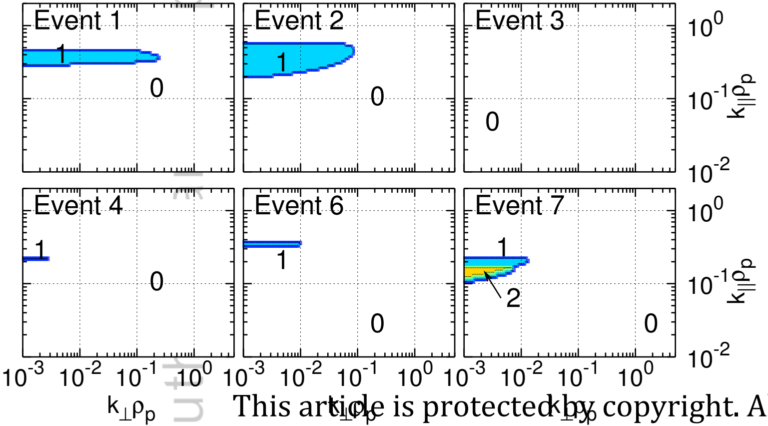
Event 1
Event 2
Event 3
Event 4
Event 6
Event 7
1
0
2
10^{-3}
10^{-2}
10^{-1}
10^{0}
$k_\perp \rho_p$
$k_{||}\rho_p$